Internal tide generation by arbitrary two-dimensional topography

PAULA ECHEVERRI† AND THOMAS PEACOCK

Department of Mechanical Engineering, Massachusetts Institute of Technology,
77 Massachusetts Avenue, Cambridge, MA 02139, USA

To date, analytical models of internal tide generation by two-dimensional ridges have considered only idealized shapes. Here, we advance the Green function approach to address the generation of internal tides by two-dimensional topography of arbitrary shape, employing the Wentzel-Kramers-Brillouin (WKB) approximation to consider the impact of non-uniform stratifications. This allows for a more accurate analytical estimation of tidal conversion rates. Studies of single and double ridges reveal that the conversion rate and the nature of the radiated internal tide can be sensitive to the topographic shape, particularly around criticality and when there is interference between wave fields generated by neighbouring ridges. The method is then applied to the study of two important internal tide generation sites, the Hawaiian and Luzon Ridges, where it captures key features of the generation process.

Key words: internal waves, stratified flows, topographic effects

---

1. Introduction

Oceanic internal tides are internal wave fields of tidal period. They are produced by barotropic tidal flow over topography, with steep, large-amplitude, nominally two-dimensional topographic features being particularly significant generators (Egbert & Ray 2000; Rudnick *et al.* 2003; Simmons, Hallberg & Arbic 2004). While some of the internal tidal energy produced by these ridges is believed to go into local mixing near the topography, the consensus is that for tall ridges a majority of the generated energy is radiated away, to participate in processes such as wave–wave interactions and reflections from the continental shelf (Ray & Mitchum 1997; Garrett & Kunze 2007; Echeverri *et al.* 2009). At the Mendocino Escarpment, for instance, field studies reveal that turbulent dissipation over the top of the topography accounts for only 1 % of the energy flux in the internal tides (Althaus, Kunze & Sanford 2003), and at Kaena Ridge in Hawaii the corresponding values are 5–25 % (Klymak, Pinkel & Rainville 2008).

Given the significant contribution to global internal tide generation by nominally two-dimensional topography, there has been a substantial effort to develop analytical models that reasonably predict internal tide conversion rates by such features. An early approach (Baines 1973) uses the method of characteristics, although this technique has proven challenging to implement. The approach of Bell (1975) uses Fourier methods to model internal tide generation by small-scale ridges in an infinitely deep ocean that

† Email address for correspondence: pauleche@gmail.com

is uniformly stratified. A key restriction is that the topography be very subcritical, i.e. $\varepsilon \ll 1$, where the criticality parameter

$$\varepsilon = \frac{h'(x)}{\tan \theta} \tag{1.1}$$

is the ratio of the topographic slope $h'(x)$ to the slope of the internal wave rays $\tan \theta = \sqrt{(N^2 - \omega^2)/(\omega^2 - f^2)}$, where ω is the forcing frequency, N is the buoyancy frequency that characterizes a density stratification and f is the background rotation; another requirement is that $h/H \ll 1$, where H is the far-field ocean depth. Llewellyn Smith & Young (2002) and Khatiwala (2003) also consider subcritical, small-amplitude ridges, but in a finite-depth ocean, the former study also accounting for non-uniform stratification via the WKB approximation.

Consideration of finite-amplitude topography in an infinitely deep ocean was achieved by Balmforth, Ierley & Young (2002) using a Fourier series-based approach that still requires the topography to be subcritical. Studies of supercritical topography in a finite-depth ocean were performed by Baines (1982) using ray tracing techniques, and by St. Laurent *et al.* (2003) and Llewellyn Smith & Young (2003), who considered idealized features such as a knife-edge and a step; the latter study also utilized the WKB approximation to investigate the effects of a non-uniform stratification. Most recently, in an effort to consider ever more realistic topography, the Green function approach of Robinson (1969) was developed to study the scenarios of polynomial and triangular ridges in a finite-depth ocean (Pétrélis, Llewellyn Smith & Young 2006), a periodic knife-edge (Nycander 2006) and Gaussian (Balmforth & Peacock 2009) topography in an infinitely deep ocean.

All the aforementioned studies considered topography that is symmetric and/or spatially periodic. Of course, this is never the case for an ocean ridge, and it remains an open issue to determine how features such as topographic asymmetry and roughness can affect internal tide generation by an isolated, two-dimensional ridge. Some initial insight is provided by the work of Griffiths & Grimshaw (2007), which considers the naturally asymmetric case of continental shelves rather than mid-ocean ridges, revealing significant differences in the shoreward and oceanward energy fluxes of the internal tide. Another situation that also merits realistic analytical modelling is a multiple-ridge system of finite extent, since results for idealized, spatially periodic topography (Nycander 2005; Balmforth & Peacock 2009) suggest that interference and scattering of the wave fields generated by neighbouring ridges can substantially affect the radiated internal tide.

In this paper, we use a Green function approach (Robinson 1969; Pétrélis *et al.* 2006) to address internal tide generation by arbitrary two-dimensional ridge geometries, which may be a single asymmetric ridge or a system of multiple ridges. In addition, the WKB approximation is employed to consider non-uniform stratifications and thus obtain some reasonable predictions for the Hawaiian and Luzon Ridges. Section 2 gives a summary of the analytical method. In §3, we present results for single and double ridges in a uniform stratification, before proceeding in §4 to case studies of the Hawaiian and Luzon Ridges, which exemplify large-amplitude complex topography in non-uniform stratification. Our conclusions are then presented in §5.

2. Theory

The streamfunction $\psi(x, z, t)$ is defined so that the baroclinic perturbation velocities of the internal tide are $(u, w) = (-\psi_z, \psi_x)$, the horizontal and vertical coordinates being

x and z, respectively. We assume a harmonic solution,

$$\psi(x, z, t) = U\text{Re}[\phi(x, z)e^{-i\omega t}], \tag{2.1}$$

produced by the background barotropic flow $U\text{Re}[e^{-i\omega t}]$ of magnitude U and frequency ω in a Boussinesq and inviscid ocean with non-uniform stratification $N(z)$ and background rotation f. The wave field is assumed linear and studied in the limit of small tidal excursion relative to the characteristic width of the topography, $1/k$, such that $kU/\omega \ll 1$. The governing equation for $\phi(x, z)$ is thus (Llewellyn Smith & Young 2003; Balmforth & Peacock 2009):

$$\left(\frac{N(z)^2 - \omega^2}{\omega^2 - f^2} \right) \frac{\partial^2 \phi}{\partial x^2} - \frac{\partial^2 \phi}{\partial z^2} = 0. \tag{2.2}$$

The sea-floor topography $h(x)$ and the ocean surface (approximated as a rigid-lid) impose the no normal-flow boundary conditions:

$$\phi(x, h(x)) = h(x), \qquad \phi(x, H) = 0, \tag{2.3}$$

where H is the far-field ocean depth.

Pursuing a solution to (2.2)–(2.3), we seek Green's function $G(x, x'; z, z')$ that solves

$$\left(\frac{N(z)^2 - \omega^2}{\omega^2 - f^2} \right) G_{xx} - G_{zz} = \delta(x - x')\delta(z - z'), \tag{2.4}$$

subject to the radiation boundary condition in x that disturbances must propagate away from x', which requires that, for a horizontal wave number k, the Green function takes the form

$$G(x, x'; z, z')e^{-i\omega t} = f(k|x - x'| - \omega t); \tag{2.5}$$

and homogeneous conditions in the vertical domain, i.e.

$$G(x, x'; (0, H), z') = 0. \tag{2.6}$$

It is convenient to introduce the dimensionless and stretched vertical coordinate

$$Z = \frac{\pi}{H\bar{N}} \int_0^z \sqrt{N(z')^2 - \omega^2} \, dz', \tag{2.7}$$

and the corresponding dimensionless horizontal coordinate

$$X = \frac{\pi x}{\mu H}, \tag{2.8}$$

where $\mu = \bar{N}/\sqrt{\omega^2 - f^2}$ and

$$\bar{N} = \frac{1}{H} \int_0^H \sqrt{N(z')^2 - \omega^2} \, dz'. \tag{2.9}$$

The WKB approximation of the Green function is

$$G(|X - X'|; Z, Z') = \sum_{p=1}^{\infty} \frac{1}{p\pi} \frac{\sin(pZ)}{\sqrt{\mathcal{N}(R(Z))}} \frac{\sin(pZ')}{\sqrt{\mathcal{N}(R(Z'))}} e^{ip|X - X'|}. \tag{2.10}$$

where

$$\mathcal{N}(Z) = \frac{1}{\bar{N}} \sqrt{N(R(Z))^2 - \omega^2} \tag{2.11}$$

and the stretched coordinate is mapped back into a physical vertical coordinate via $z = R(Z)$. This approximation is valid for stratifications that vary slowly with respect

to the vertical scale of the internal waves and, while it is most accurate for short vertical wavelengths, it does not give misleading data even for the longest wavelength solutions (Llewellyn Smith & Young 2002). In the limit of a uniform stratification, the WKB solution is exact, $\bar{N} = \sqrt{N^2 - \omega^2}$, $Z = \pi z/H$, $\mathcal{N}(z) = 1$, and (2.10) reduces to the Green function of Robinson (1969) and Pétrélis *et al.* (2006).

A distribution of singularities $\gamma(X)$ along the non-dimensional topography $\hat{h}(X) = \pi h(x)/H$ is used to account for internal tide generation, the wave field being given by

$$\phi(X, Z) = \frac{H}{\pi} \int_{-a}^{b} \gamma(X') G(|X - X'|; Z, \hat{h}(X')) \, dX', \qquad (2.12)$$

where it is assumed that the topography is of arbitrary shape within $X \in [-a, b]$ and of zero height elsewhere. Solution (2.12) differs from that of Pétrélis *et al.* (2006) as it considers a horizontally, rather than vertically, distributed array of sources (i.e. $\gamma(X)$ instead of $\gamma(Z)$), which is the key to straightforwardly handling problems with complex topography. This approach was also used by Balmforth & Peacock (2009), but in this study we remove their assumptions of symmetry or periodicity.

The desired quantity $\gamma(X)$ is found by imposing the lower boundary condition in (2.3) and solving the integral equation

$$h(X) = \frac{H}{\pi} \int_{-a}^{b} \gamma(X') G(|X - X'|; \hat{h}(X), \hat{h}(X')) \, dX'. \qquad (2.13)$$

Our numerical approach to solving this problem, which is less sophisticated but perhaps more transparent than that of Pétrélis *et al.* (2006), is detailed in the Appendix. We tested our solution method by comparing with the results of Balmforth *et al.* (2002), Llewellyn Smith & Young (2003), Pétrélis *et al.* (2006) and Balmforth & Peacock (2009), obtaining excellent agreement in the different respective limits of all of these approaches.

In the far field, where $X < -a$ or $X > b$, one can define:

$$\gamma_p^{\pm} = \frac{1}{\pi} \int_{-a}^{b} \gamma(X') \frac{\sin(p\hat{h}(X'))}{\sqrt{\mathcal{N}(\hat{h}(X'))}} e^{\mp i p X'} dX', \qquad (2.14)$$

where the superscript of $\gamma_p^{\pm}$ indicates left $(-)$ and right $(+)$ going waves, respectively, such that, in the far field, the solution of (2.12) can be written as

$$\phi^{\pm}(X, Z) = \frac{H}{\pi} \sum_{p=1}^{\infty} \frac{\gamma_p^{\pm}}{p} \frac{\sin(pZ)}{\sqrt{\mathcal{N}(R(Z))}} e^{\pm i p X}. \qquad (2.15)$$

The conversion rate $C^{\pm}$, which is the depth-integrated radiated energy flux to the left $(-)$ and right $(+)$ of the topography, can be expressed in terms of $\gamma_p^{\pm}$ (Pétrélis *et al.* 2006) as

$$C^{\pm} = \pm \frac{\bar{\rho} U^2 H^2 \bar{N}^2}{4\pi\mu\omega} \sum_p^{\infty} \frac{|\gamma_p^{\pm}|^2}{p} = \pm \frac{\bar{\rho} U^2 H^2 \bar{N}^2}{4\pi\mu\omega} C_*^{\pm}, \qquad (2.16)$$

where $C_* = \sum_p^{\infty} (|\gamma_p|^2/p)$ is the non-dimensional conversion rate and $\bar{\rho}$ is a reference background density.
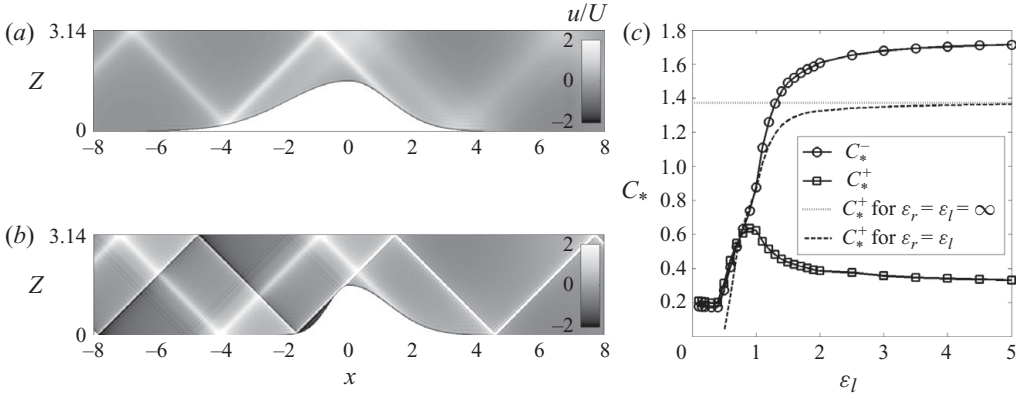
FIGURE 1. Snapshots of u/U for internal tides generated by asymmetric Gaussian ridges with $h_0/H = 0.5$, $\varepsilon_r = 0.75$ and (*a*) $\varepsilon_l = 0.5$ and (*b*) $\varepsilon_l = 1.5$. (*c*) Non-dimensional conversion rate in each direction, $C_*^\pm$, as a function of ε_l for $\varepsilon_r = 0.75$, for a symmetric ridge ($\varepsilon_r = \varepsilon_l$), and for a knife-edge ($\varepsilon_r = \varepsilon_l \to \infty$).

3. Uniform stratification

3.1. *An isolated ridge*

We begin by considering an asymmetric Gaussian ridge:

$$h_G(x) = \frac{h_0}{1 - e^{-8}} \begin{cases} \exp\left(-\dfrac{x^2}{2\sigma_l^2}\right) - e^{-8} & -4\sigma_l \leqslant x \leqslant 0, \\[2mm] \exp\left(-\dfrac{x^2}{2\sigma_r^2}\right) - e^{-8} & 0 < x \leqslant 4\sigma_r, \\[2mm] 0 & x < -4\sigma_l, \quad x > 4\sigma_r, \end{cases} \tag{3.1}$$

where h_0 is the maximum height, and $2\sigma_l$ and $2\sigma_r$ are the characteristic widths of the left and right sides of the ridge, respectively. The factor $1 - e^{-8}$ ensures that the topography goes continuously, but not smoothly, to zero height at $-4\sigma_l$ and at $4\sigma_r$. The slopes on either side of the ridge are different, so the criticality on the left side of the ridge, $\varepsilon_l = \max(h'_G \in [x = -4\sigma_l : 0])/\tan\theta$, differs from that on the right, $\varepsilon_r = \max(|h'_G \in [x = 0 : 4\sigma_r]|)/\tan\theta$.

Figures 1(*a*) and 1(*b*), respectively, present snapshots of the normalized horizontal velocity u/U for wave fields generated by an asymmetric Gaussian ridge with depth ratio $h_0/H = 0.5$, $\varepsilon_r = 0.75$ and $\varepsilon_l = 0.5$ and 1.5. In figure 1(*a*), both sides of the ridge are subcritical, so both left- and right-going wave fields possess beams propagating away from the opposite side of the ridge. The beam propagating to the left, which is generated on the steeper right slope, is sharper, containing finer vertical structure and a larger peak amplitude. In addition to these, there are waves in each direction (propagating leftward from the left slope and rightward from the right slope) that are not so readily visible but still contain significant energy flux. In figure 1(*b*), the left side of the ridge is supercritical. Two wave beams are generated at the upper critical point of the left slope, one radiating up-and-right and the other radiating down-and-left, causing the far-field structure to be markedly different to the right and left of the ridge. In the right far field there is a single sharp right-propagating beam, whereas in the left far field there are two left-propagating wave beams, the sharper beam originating from the left side of the ridge and the broader beam coming from the right side. Formally, there is a singularity in the wave field associated with the sharp
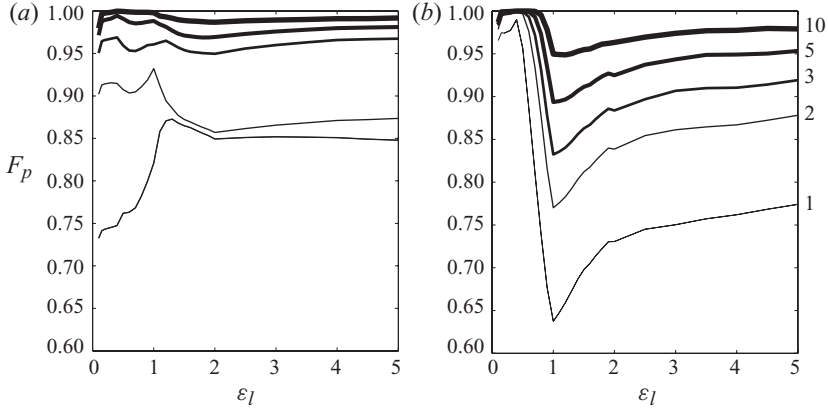
FIGURE 2. Fraction F_p of the far-field conversion in the first p modes to the (*a*) left and (*b*) right of the asymmetric ridge in figure 1(*a*). Results are shown for $p = 1, 2, 3, 5$ and 10, with the value of p increasing with line thickness, and also indicated on the right side of (*b*).

beams originating from the critical slope. In practice, this has been circumvented by plotting the wave field using a sum of only the first 50 modes, which was sufficient for convergence of the energy flux.

Figure 1(*c*) presents the dimensionless conversion rates $C_*^{\pm}$ for the wave fields in figures 1(*a*) and 1(*b*) as a function of ε_l, which was varied by changing σ_l while keeping all other parameters constant. In the limit $\varepsilon_l \to 0$, we expect the energy flux to be generated only by the right slope. However, as ε_l decreases, it is increasingly difficult to evaluate the solution $\gamma(X)$ because the horizontal domain $[-a : b]$ increases and the size of the computation scales as the horizontal domain squared, as per (2.13) and (A 6). Towards this limit, however, we find that the energy flux is basically symmetric, although closer inspection of the results in figure 1(*c*) reveals that slightly more energy goes to the right than to the left. In the limits $\varepsilon_l \to 0$ and $\varepsilon_r \to 0$, the energy radiation is symmetric regardless of the topographic shape (Llewellyn Smith & Young 2002).

As ε_l approaches criticality, the value of C_*^- increases rapidly and monotonically with ε_l for $\varepsilon_l < 1.5$, with a notable rise in the rate of increase at criticality. The rate of ascent then diminishes for $\varepsilon_l > 1.5$, and for $\varepsilon_l \geqslant 5$ the conversion rate is essentially constant. The value of C_*^+ also initially increases with criticality for $\varepsilon_l < 1$. For $\varepsilon_l > 1$, however, there is initially a sharp decrease in C_*^+, beyond which the conversion rate eventually settles to a constant value. The decrease in the rightward energy flux coincides with the appearance of the second leftward-propagating wave beam from the left-hand slope for $\varepsilon_l \geqslant 1$, and the same trend at criticality was consistently observed for both sub- and supercritical values of ε_r. Also included in figure 1(*c*) is the conversion rate for a symmetric ridge ($\varepsilon_r = \varepsilon_l$), which is the same to the left and right, and which approaches the limiting value of a knife-edge for $\varepsilon \geqslant 5$. This limiting value is actually less than that of C_*^-, revealing that the directional conversion rate of an asymmetric ridge can exceed that of a sharper symmetric ridge. However, the total conversion rate of the asymmetric ridge, this being the sum of the left- and right-going energy fluxes, is lower than that of the knife-edge, which is double the value presented in figure 1(*c*).

Figure 2 presents F_p, the fraction of the far-field conversion in the first p modes radiated by the ridge in figure 1(*a*), as a function of ε_l. Here,

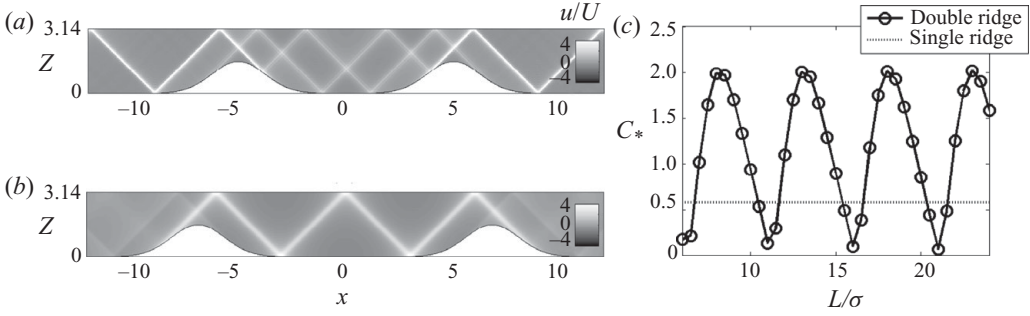$$F_p^{\pm} = \frac{1}{C_*^{\pm}} \sum_{n=1}^{p} \frac{|\gamma_n^{\pm}|^2}{n}, \qquad (3.2)$$

FIGURE 3. Snapshots of u/U for internal tides generated by two identical Gaussian ridges with $h_1/H = h_2/H = 0.5$, $\varepsilon_1 = \varepsilon_2 = 0.75$ and (a) $L/\sigma = 8.2$ and (b) $L/\sigma = 11.2$. (c) Non-dimensional conversion rate to either direction C_* as a function of L/σ. The dotted line shows C_* for a single ridge.

and ε_l was again increased by decreasing σ_l. Although $F_p^{\pm}$ are dominated by mode 1, which always carries more than 60 % of the energy flux, the modal structures of the wave fields propagating to the left and right are quite different. Furthermore, as ε_l transitions from sub- to supercritical, there are sharp changes in the modal structure in both directions, coinciding with the appearance of a new left-going wave beam. For the left-going wave field, the relative contribution of mode 1 increases and mode 2 becomes much less significant than mode 3. Conversely, for the right-going wave field, the contribution from mode 1 drops sharply around criticality, where the higher modes become much more significant.

3.2. *A double ridge*

For a double-ridge system, we consider the sum of two Gaussian ridges $h_D(x) = h_{1G}(x) + h_{2G}(x)$, where

$$
\left.
\begin{aligned}
h_{1G}(x) &= \frac{h_1}{1 - e^{-8}} \left[\exp\left(-\frac{(x + L/2)^2}{2\sigma_1^2} \right) - e^{-8} \right], \quad -L/2 - 4\sigma_1 < x < -L/2 + 4\sigma_1, \\
h_{2G}(x) &= \frac{h_2}{1 - e^{-8}} \left[\exp\left(-\frac{(x - L/2)^2}{2\sigma_2^2} \right) - e^{-8} \right], \quad L/2 - 4\sigma_2 < x < L/2 + 4\sigma_2,
\end{aligned}
\right\}
$$
(3.3)

and $h_D = 0$ elsewhere. Here, L is the separation between the two ridge peaks and $4\sigma_1$ and $4\sigma_2$ are the characteristic full widths of the left and right ridges, respectively.

For a pair of subcritical Gaussian ridges, the internal tide radiated by one of the ridges interferes with that radiated by the other, and is also scattered by the neighbouring ridge, but cannot be reflected back. Figures 3(a) and 3(b) present u/U for wave fields generated by two identical, subcritical Gaussian ridges with $h_1/H = h_2/H = 0.5$, $\varepsilon_1 = \varepsilon_2 = 0.75$ and $L/\sigma = 8.2$ and $L/\sigma = 11.2$, respectively. The radiated wave field is substantially different for the two scenarios. A single strong wave beam radiates to each side for $L/\sigma = 8.2$ (figure 3a). In contrast, for $L/\sigma = 11.2$, two weak beams radiate away in each direction, and there is intense activity between the ridges (figure 3b).

Figure 3(c) presents C_*, evaluated using the first 50 modes, as a function of L/σ. For comparison, the conversion rate for an individual ridge is also included in this figure. The first maximum in the periodic sequence is for $L/\sigma = 8.2$, which corresponds to constructive interference of the wave fields generated by the two ridges. For this scenario, presented in figure 3(a), one can follow the rightward-propagating wave
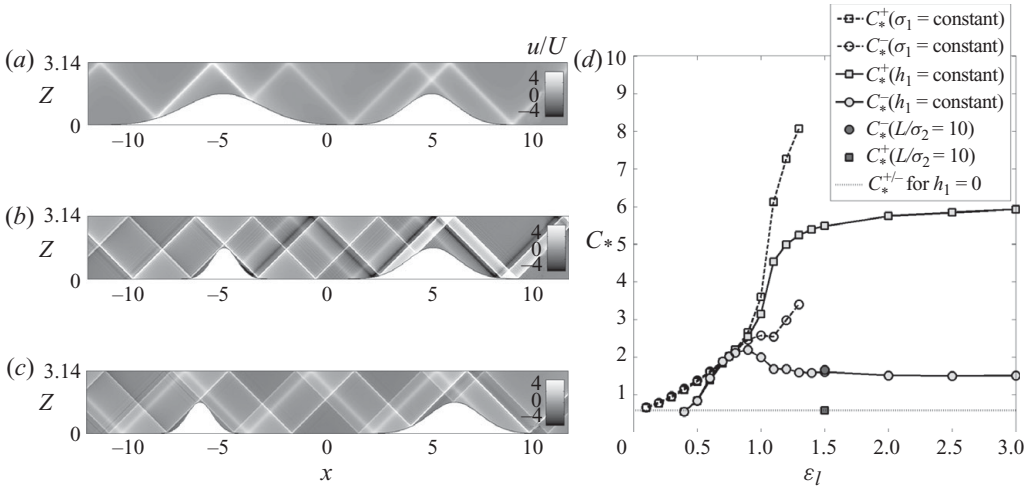
FIGURE 4. Snapshots of u/U for internal tides generated by a double ridge with $h_1/H = h_2/H = 0.5$, $\varepsilon_2 = 0.75$, $L/\sigma_2 = 8.2$ and (a) $\varepsilon_1 = 0.5$, and (b) $\varepsilon_1 = 1.5$. (c) The same as (b) except $L/\sigma_* = 10$. (d) $C_*^{\pm}$ as a function of ε_1, where ε_1 is varied by changing σ_1 (solid lines) and h_1 (dashed lines). All results are for $L/\sigma_2 = 8.2$ unless otherwise indicated in the caption.

beam originating on the outside of the left ridge to the inside of the right ridge, where it reflects in-phase with the locally generated rightward-propagating wave beam. In contrast, for $L/\sigma = 11.2$, the wave beams generated on the outside of each ridge destructively interfere outside the confines of the ridges, as shown in figure 3(b), corresponding to a minimum in the periodic sequence of C_*. This periodic sequence of constructive and destructive interference has been previously reported in systems with periodic topography in infinitely deep oceans (Nycander 2005; Balmforth & Peacock 2009). We find similar trends even for ridges that are substantially more subcritical, which do not generate sharp wave beams, and if other parameters, such as h/H, are systematically varied.

If the ridges in a double-ridge system differ in shape, it is reasonable to expect the radiated internal tide to be asymmetric. As an example, the normalized horizontal velocity fields for a pair of Gaussian ridges with $h_1/H = h_2/H = 0.5$, $L/\sigma_2 = 8.2$, $\varepsilon_2 = 0.75$ and $\varepsilon_1 = 0.5$ and 1.5 are presented in figures 4(a) and 4(b), respectively, the criticality ε_1 being changed by virtue of changing σ_1. When both ridges are subcritical the left- and right-going fields are qualitatively similar, as shown in figure 4(a). However, when the left ridge is supercritical, as in figure 4(b), a distinct asymmetry is apparent. The far-field internal tide is dominated in both directions by sharp wave beams generated at the supercritical ridge, the asymmetry arising because the rightward-propagating wave beams reflect at different locations on the subcritical ridge, bringing them closer to one another. Another contributing factor to the asymmetry, albeit a weaker one, is the initially leftward-propagating wave beam from the subcritical ridge being reflected back to the right by the supercritical slope it encounters.

As is the case for a symmetric double ridge (figure 3), the nature of the radiated tide for an asymmetric double-ridge system depends sensitively on the ridge geometry. Figure 4(b) shows a noticeably stronger tide than figure 4(c), yet the only difference between the two is a change in L/σ_2 from 8.2 to 10. This relatively small change,
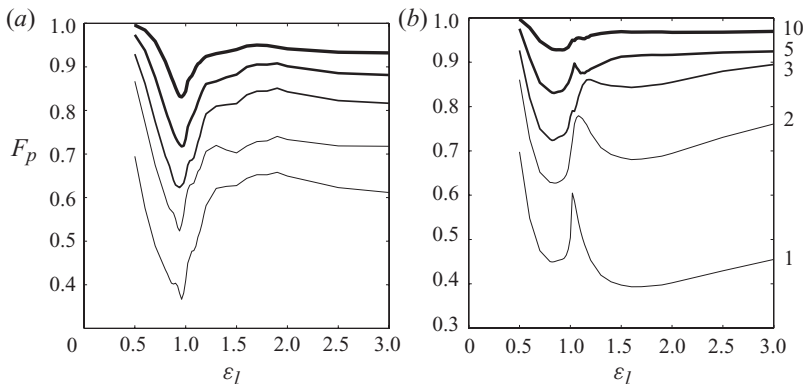
FIGURE 5. Fraction F_p of the far-field conversion in $p = 1, 2, 3, 5$ and 10 modes to the (a) left and (b) right of the double ridge in figure 4(a).

however, has important geometric consequences. In contrast to the wave field in figure 4(b), for example, the leftward-propagating wave beam originating on the outer slope of the right ridge in figure 4(c) no longer encounters the left ridge, significantly altering wave structure in the left far field.

To further demonstrate the impact of geometric asymmetry on the radiated internal tide, figure 4(d) presents $C_*^{\pm}$ as a function of ε_1, evaluated using 50 modes, where ε_1 is increased by either decreasing σ_1 (as in figures 4a and 4b) or increasing h_1. Although asymmetry in the conversion rate is most obvious when the left ridge is supercritical, there is some asymmetry when both ridges are subcritical. The results for increasing values of h_1 are truncated at $\varepsilon_1 = 1.4$ since C_* diverges as h_1/H approaches 1. There is a temptation to assume that C_*^{+} will always exceed C_*^{-} provided the left ridge is supercritical, because the supercritical ridge can reflect energy back to the right. This is not so, however, as the stronger energy flux is towards the left for the configuration in figure 4(c), as indicated in figure 4(d). Finally, we note that for all the subcritical scenarios we studied, the conversion rate is symmetric and approaches that of the individual right ridge (particularly if ε_1 is reduced by reducing h_1). This is because when both ridges are subcritical, the wave beams produced are broad and insensitive to the asymmetry of the topography, i.e. the two left-going wave beams basically interact in the same way as the two right-going wave beams. It is only near criticality, where the wave beams become sharp relative to the scale of the topography, that asymmetry emerges in the results.

Figure 5 presents F_p for the wave field radiated by the double-ridge system in figure 4(a) as ε_1 is increased by decreasing σ_1. The radiated modal structure on the left and right is qualitatively and quantitatively very similar for $\varepsilon_1 \leqslant 1$, which is expected since the far-field structure in both directions is dominated by a single wave beam of like amplitude. For $\varepsilon \simeq 1$ the relative contribution of mode 1 dips to less than half for the left-going wave field but peaks for the right-going wave field. For $\varepsilon_1 > 1$, however, this trend is reversed, and a notable feature is that mode 2 contributes far more significantly to the rightward than leftward energy flux.

4. Non-uniform stratification

Having investigated single and double ridges in uniform stratifications, finding that asymmetry in both the energy flux and modal structure can be sensitive to the
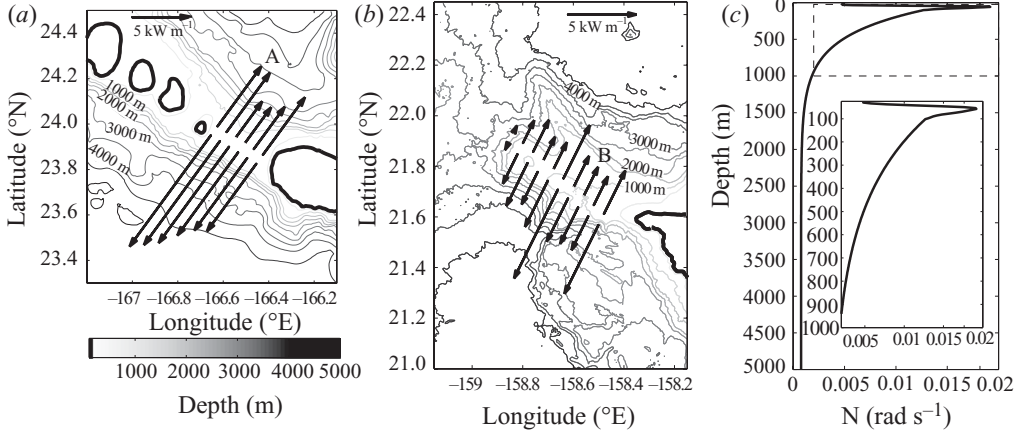
FIGURE 6. Bathymetry of (*a*) the ridge at French Frigate Shoals and (*b*) the Kaena Ridge. The vectors in (*a*) and (*b*) are proportional to the two-dimensional energy flux evaluated at 6 cross-sections of French Frigate Shoals and 10 cross-sections of Kaena Ridge. The stratification presented in (*c*) is from averaged HOTS CTD casts, with a zoom-in of the stratification in the upper 1000 m (inset).

topographic shape, we proceed to investigate more realistic single and double ridges in non-uniform stratifications, using the Hawaiian and Luzon Ridges, respectively, as examples. These studies are somewhat idealized, as they assume two-dimensional flow for cross-sections of the ridges and employ the WKB approximation to account for a non-uniform background stratification, which is least accurate for the lowest mode. Nevertheless, this is a significant advance on previous analytical studies as it incorporates both realistic topography and stratification. Herein, we proceed to investigate the predictions of the analytical model for these two geographical locations, and make comparisons with the results of relevant numerical simulations and field data.

4.1. *Hawaiian Ridge*

Figures 6(*a*) and 6(*b*) show the bathymetry of the ridge between French Frigate Shoals and Brooks Banks, and of Kaena Ridge in the Kauai Channel, respectively. The bathymetry for French Frigate Shoals was obtained from the latest, satellite-derived marine topography release SRTM30_PLUS (Becker *et al.* 2009), and the bathymetry data for Kaena Ridge was obtained from multibeam data compiled by the Hawaiian Mapping Research Group (2009). Internal tide generation was modelled at six evenly spaced, 120 km-long cross-sections at French Frigate Shoals, and 10 evenly spaced, 140 km long cross-sections at Kaena Ridge. For each cross-section, $h(x)$ was obtained by fitting the bathymetry every 1.4 km with a spline and interpolating to obtain a smooth shape sampled every 70 m. The same sample stratification $N(z)$ was used for both locations, since there is not much spatial variability in the averaged stratifications for French Frigate Shoals and Kaena Ridge (Klymak *et al.* 2006). The stratification, presented in figure 6(*c*), was based on an average of thirty 1100 m deep CTD casts in the Hawaiian Ocean time-series (HOT) database taken at 24 h intervals during September 2000 in the Kauai Channel. The profile for the upper 100 m is an interpolated spline of the HOT stratification, while for the bottom 4900 m, it is an exponential fit to the values of the measured stratification at depths of 100, 300 and 1050 m. A similar exponential fit was used by Llewellyn Smith & Young (2003). It is possible to use stratifications that retain more of the fine structure of the ocean data (e.g. a weak secondary thermocline around 300 m), but we choose to work with this

	French Frigate Shoals			Kaena Ridge			
	Present study	M&H	Lee *et al.*	Present study	M&H	Carter *et al.*	Nash *et al.*
C^-	12.1	~15	~21	7.8	~10	~6.1	~17
C^+	6.5	~10	~7.5	4.7	~8	~5.0	–

TABLE 1. Estimates of the maximum energy flux $C^\pm$ in kW m^{-1} at the Hawaiian Ridge. The results of the present study are compared with those of Merrifield & Holloway (2002, abbreviated as M&H), Carter *et al.* (2008), Lee *et al.* (2006) and Nash *et al.* (2006).

simpler version that captures the primary thermocline, which is the key feature of the stratification.

The two-dimensional, far-field conversion rate $C^\pm$, where '−' indicates southwest and '+' indicates northeast, was calculated for each cross-section in figure 6(*a*) using 100 modes, with $\bar{\rho} = 1010$ kg m^{-3} and H, μ and $\bar{N}$ evaluated at each cross-section using $\omega = 1.4 \times 10^{-4}$ rad s^{-1} and $f = 5 \times 10^{-5}$ rad s^{-1}. For the purpose of this study, a reasonable value of the far-field barotropic velocity was $U = 2$ cm s^{-1}, which lies between the smallest value of $U = 1$ cm s^{-1}, used in numerical and analytical studies (Merrifield & Holloway 2002; Llewellyn Smith & Young 2003), and the larger value $U = 3$–4 cm s^{-1}, reported in field studies (St. Laurent & Nash 2004; Lee *et al.* 2006). Since the magnitude of C scales with U^2 (equation (2.16)), this introduces significant uncertainty into the predicted conversion rates, which can only be reasonably estimated within the bounds set by the uncertainty in U.

The values of $C^\pm$, represented by the vectors on figures 6(*a*) and (*b*), vary over 4.0–12.1 kW m^{-1} at French Frigate Shoals and 0.4–7.8 kW m^{-1} at Kaena Ridge. At Kaena Ridge, the maximum conversion rate occurs at the southern end of the ridge, where the depth ratio approaches 0.9. Further southeast, where the depth ratio exceeds 0.9, we expect the flow to be three-dimensional, preferring to go around rather than over the ridge, and two-dimensional linear theory is unlikely to provide a reasonable estimate of the tidal conversion. The peak magnitudes of the predicted conversion rates at both French Frigate Shoals and Kaena Ridge are in good agreement with the results of three-dimensional numerical simulations of Merrifield & Holloway 2002, which predict $C^- \approx 15$ kW m^{-1} and $C^+ \approx 10$ kW m^{-1} for French Frigate Shoals, and $C^- \approx 10$ kW m^{-1} and $C^+ \approx 8$ kW m^{-1} for Kaena Ridge; and the three-dimensional numerical simulations of Carter *et al.* (2008), which predict $C^- \approx 6.1$ kW m^{-1} and $C^+ \approx 5.0$ kW m^{-1} for Kaena Ridge. This is also consistent with field data, which estimate $C^- \approx 21$ kW m^{-1} and $C^+ \approx 7.5$ kW m^{-1} for French Frigate Shoals and $C^- \approx 17$ kW m^{-1} for Kaena Ridge (Lee *et al.* 2006; Nash *et al.* 2006). These comparisons are summarized in table 1.

While the quantitative values of the theoretical conversion rates have inherent uncertainty due to the quadratic dependence of C on U, an important qualitative feature that is well captured by the analytic model is the asymmetry of the energy flux from both French Frigate Shoals and Kaena Ridge. The results in figures 6(*a*) and 6(*b*) show that, for both locations, the internal tide radiated to the southwest is predicted to be appreciably stronger than that to the northeast, which is also a feature of the data from field studies and numerics (see figure 1 in Lee *et al.* 2006, figure 6 in Merrifield & Holloway 2002 and figure 7 in Carter *et al.* 2008).

Figure 7 presents snapshots of u/U along sections A and B in figures 6(*a*) and 6(*b*), respectively. Internal wave beams propagate away from the steep slopes of the topography and are refracted by the stratification, such that, as they approach the
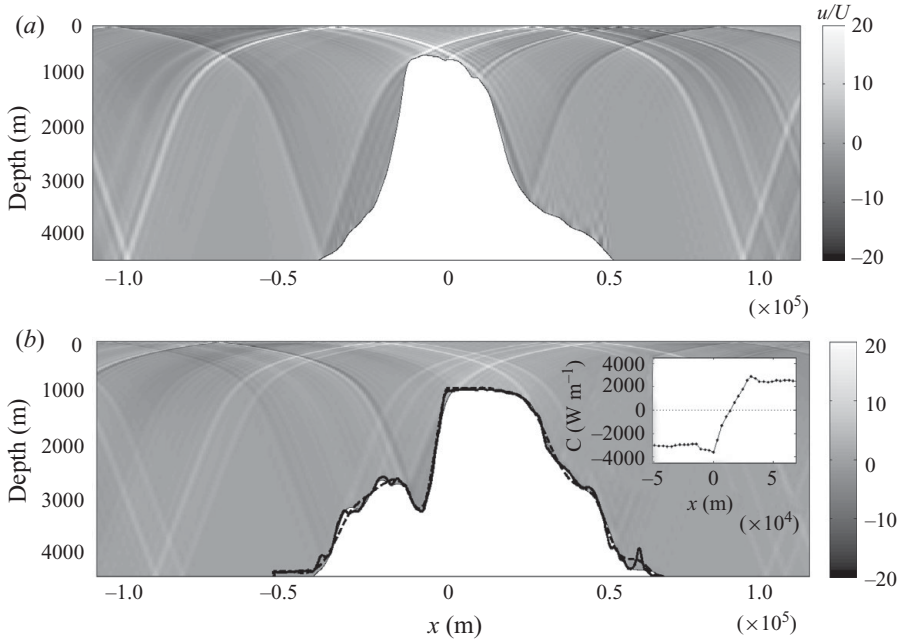
FIGURE 7. Normalized across-ridge velocity fields (u/U) generated at cross-sections (*a*) A and (*b*) B in figure 6. The thick lines in (*b*) indicate the raw bathymetry data (solid) and a smoothed version of the profile (dashed), and the inset presents the local depth-integrated, time-averaged, across-ridge energy flux. The horizontal coordinate *x* is oriented in the southwest to northeast direction.

thermocline, they become broader and more horizontal. In cross-section A (figure 7*a*), the ridge has a shallow peak at a depth of 800 m, with one inflexion point on the southwest side that otherwise has a uniform steep slope, and some roughness on the northeast side associated with several points of high criticality. There are four principal wave beams generated, two on each side of the peak, and a couple of notable, but weaker, northeast propagating beams generated by the rough features on the northeast slope. Cross-section B (figure 7*b*) coincides with the cross-sectional cut presented by Carter *et al.* (2008) (figure 5*c*). Here, the topography has steep supercritical slopes (particularly the southwest face) and a relatively flat peak at a depth of 1000 m. A pair of wave beams, one upward- and the other downward-propagating, originate from each side of the peak and overall the analytical wave field is qualitatively remarkably similar to the numerical results of Carter *et al.* (2008); for example, both predict upward beams from the different sides of the ridge peak striking the surface near $x = -40$ km, and clear downward beams near both flanks of the ridge and striking the sea floor around $x = \pm 100$ km. Cross-section B also coincides with the location of field observations by Nash *et al.* (2006) and Rainville & Pinkel (2006). Nash *et al.* (2006) discerned two internal wave beams propagating southwest from the plateau, while Rainville & Pinkel (2006) reported upward barotropic-to-baroclinic conversion over the plateau, associated with the two upward-propagating internal wave beams generated at either flank.

For cross-section A, 71 % of C^- is due to mode 1, which is seven times larger than the 10 % contribution of mode 2. Lee *et al.* (2006) also report a highly dominant mode 1 propagating southwest at this location, being about 10 times larger than

	Cross-section A		Cross-section B	
	Present study	Lee *et al.*	Present study	Nash *et al.*
F_1	71 %	∼77 %	51 %	∼65 %
F_2	10 %	∼7 %	27 %	∼31 %

TABLE 2. Estimates of the fraction F_p of the southwest energy flux C^- for modes $p = 1$ and 2 at the Hawaiian Ridge. The results of the present study are compared with those of Lee *et al.* (2006) and Nash *et al.* (2006).

the contribution of mode 2. At cross-section B we find that mode 1 accounts for 51 %, and mode 2 for 27 %, of C^-, which is in accord with the field data of Nash *et al.* (2006), who attribute ∼ 65 % of the southwest energy flux to mode 1 and ∼ 31 % to mode 2. These comparisons are summarized in table 2. The inset in figure 7(*b*) presents the depth-integrated and time-averaged across-ridge energy flux as a function of cross-ridge position for transect B. This plot further clarifies the earlier statement that in the far-field C^- is stronger than C^+. For this transect, C^- is stronger by 24 %. Nash *et al.* (2006) found the energy flux to be zero atop much of the plateau, suggesting a standing wave pattern due to the super-position of nearly symmetric wave beams generated at either flank of the ridge. We also find a reduced energy flux that approaches zero atop the ridge, but only near the centre of the plateau.

The aforementioned analysis was performed using a mildly smoothed version of the original bathymetric data, indicated by the solid thin (smoothed) and thick (original) black lines outlining the topography in figure 7(*b*). The conversion rates calculated using the smoothed data varied by only 1 % from those calculated using the original data. The dashed black line in figure 7(*b*), however, shows a yet smoother fit to the topography, a spline being fitted every 4 km and interpolated to every 40 m. This slightly smoother representation yields 15 % greater value of C^-, although only about 1 % lower value of C^+, due to the fact that the supercritical feature on the northeast slope has been modified. This result supports the assertion of Nycander (2005) that an important issue in the computation of internal tide generation is topographic resolution. As noted earlier in this study, however, for two-dimensional topography the greatest uncertainty would seem to come from the barotropic velocity U.

4.2. *Luzon Strait*

Figure 8(*a*) shows the bathymetry of Luzon Strait obtained from the ETOPO2 model of the National Geographic Data Center (2006). The two dominant features are the substantial Lan-Yu Ridge to the east that extends from north to south across the entire strait, and Heng-Chun Ridge to the west that becomes much less significant at the southern end of the strait. In comparison to the sections of Hawaiian Ridge studied in the previous section, Luzon Strait bathymetry is generally a bit shallower and more intricate, making the associated barotropic flow more three-dimensional and the region less amenable to two-dimensional analytic study. Nevertheless, we follow the lead of Chao *et al.* (2007) and investigate the two-dimensional cross-sections marked A, B and C in figure 8(*a*), at 19.97° N, 21.15° N and 21.39° N, respectively, to assess the impact of the west ridge on the internal tide radiated to the west. Towards the south, where the west ridge is relatively deep, internal tide generation by the east ridge is expected to dominate. At northern sections, where the depth ratios of the west and east ridges are similar, the west ridge is expected to play a more significant
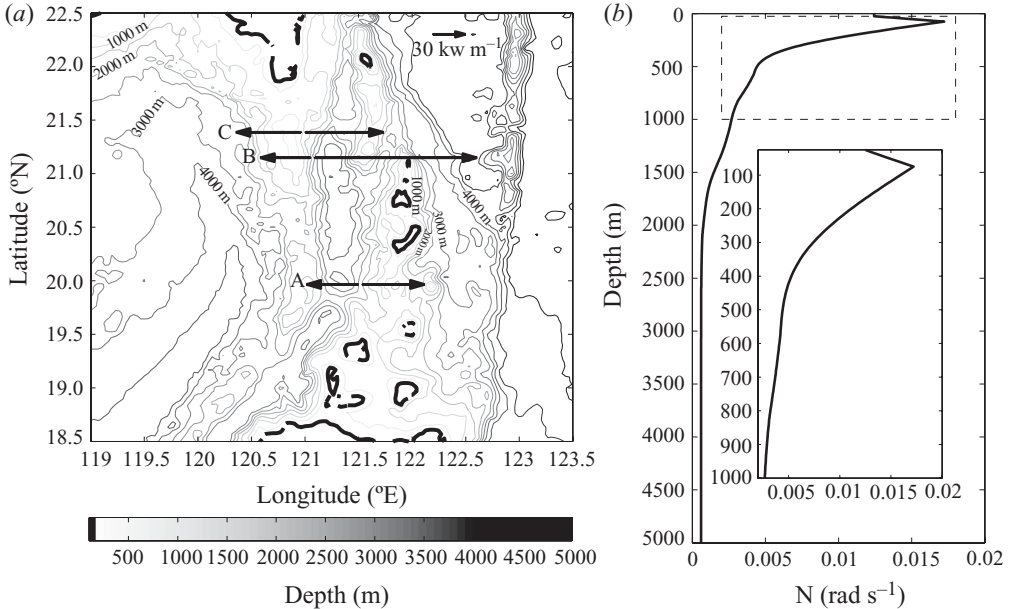
FIGURE 8. (a) Bathymetry and (b) stratification of the Luzon Strait. The vectors in (a) are proportional to the two-dimensional energy flux evaluated at three representative cross-sections labelled A, B and C.

role. Figure 8(b) shows the stratification $N(z)$ used in the model. This was obtained from an average profile of 2575 m deep CTD casts from April and July of 2007 (Farmer, Li & Park 2010) using an interpolated spline of the available stratification and an exponential fit as in §4.1.

The two-dimensional far-field conversion $C^{\pm}$, where '−' corresponds to west and '+' to east, was calculated for cross-sections A, B and C using the same parameters as for the Hawaiian Ridge (i.e. the semidiurnal tide), with the exception of $U = 5\,\mathrm{cm\,s^{-1}}$ (Niwa & Hibiya 2004; Chao et al. 2007; Jan, Lien & Ting 2008). The topography used in the calculations was found by fitting the bathymetry every 10 km with a spline and re-sampling the fit using interpolation every 100 m. Qualitatively, our results show that the internal tide radiated at cross-sections A and B is significantly stronger than that radiated at cross-section C. The conversion rates, which are highly influenced by the quadratic dependence of C on U, are $O(10\text{–}100\,\mathrm{kW\,m^{-1}})$, and are consistent with the numerical results of Niwa & Hibiya (2004) and Jan et al. (2008). The analytical model predicts unrealistically high energy fluxes for latitudes such as $20.5°$ N (the Batan Islands) where the depth ratio of the east ridge approaches unity. These unphysical results, however, could nevertheless be important indicators of generation hotspots.

A snapshot of u/U for the internal tide at cross-section B is presented in figure 9(a). A standout feature is the strong, west-propagating wave beam produced by constructive interference between two other wave beams, one generated at each of the twin peaks of the east ridge. Figure 9(b) reveals that reducing the height of the west ridge by 20% causes this constructive interference to no longer happen, so this wave beam is notably weaker in the far field. Another wave beam from the easternmost peak, which is otherwise reflected back by the supercritical slope of the west ridge, continues to propagate west, significantly altering the character of the westward internal tide.
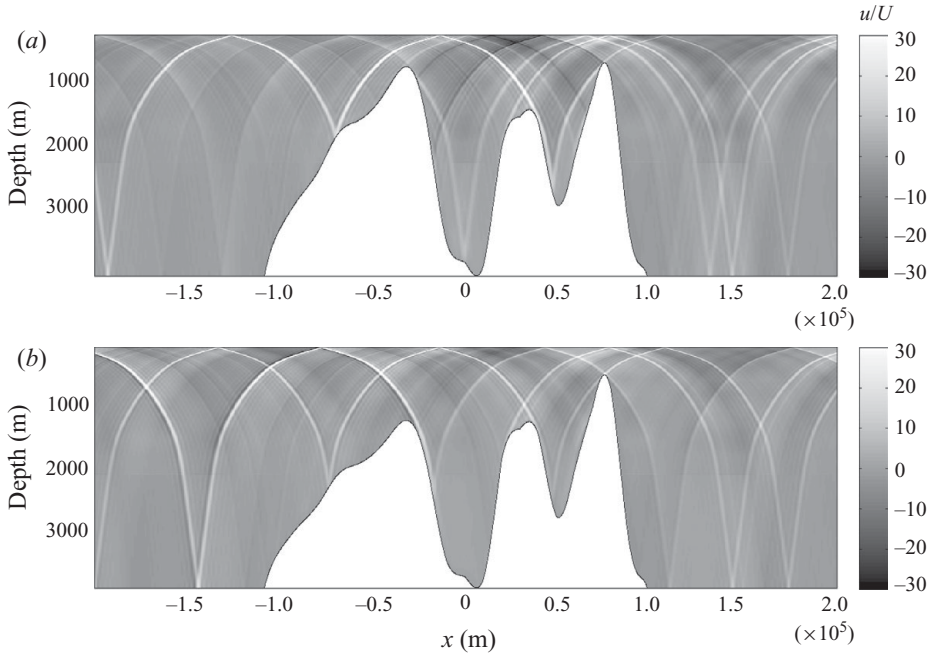
FIGURE 9. Snapshot of the normalized across-ridge velocity u/U fields for cross-section B with (*a*) full-height and (*b*) 80 %-height versions of the west ridge. The horizontal axes are aligned west to east.
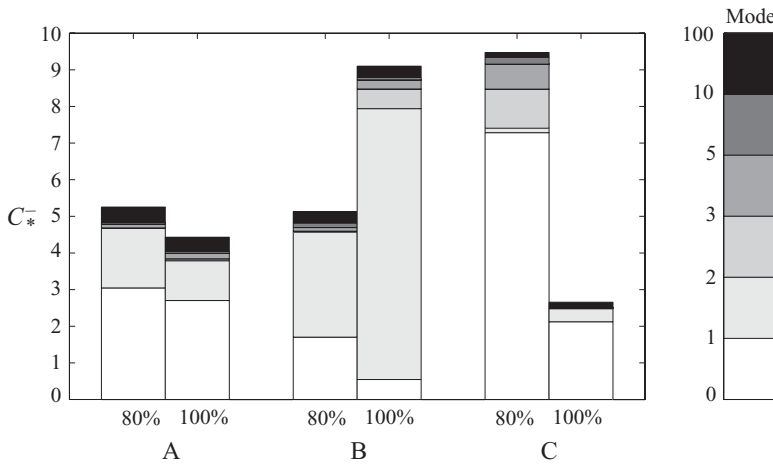

FIGURE 10. Dimensionless conversion rates C_*^- at locations A, B and C for the case in which the western ridge is at 100 % and 80 % of its true height. The fraction of the conversion rate in modes $p = 1, 2, 3, 5, 10$ and $p > 10$ is indicated within each bar.

Figure 10 summarizes the effect on the westward internal tide of decreasing the height of the west ridge by 20 % for all three cross-sections. The bar height represents the dimensionless conversion rate C_*^-, and each bar is decomposed into contributions from the different vertical modes. The energy flux at cross-sections A and C is dominated by mode 1, but at cross-section B it is mode 2 that dominates, which is surprising, because on an inspection cross-section B does not differ so dramatically in

form from cross-section A. Reducing the height of the west ridge reduces C^- for both A and C, dramatically so for C, but substantially increases C^- for cross-section B. Consistent with the results of Chao *et al.* (2007), we therefore conclude that, at the southern end of Luzon Strait, the west ridge plays a relatively minor role in internal tide generation due to its small size, whereas further north its role is more substantial. Their conclusion that, at northern latitudes, the west ridge augments the westward internal tide seems to be too sweeping a generalization, however, as we find the opposite to be true for cross-section B. Rather, the nature of the radiated internal tide depends very sensitively on the bathymetry and stratification, and needs to be assessed on a case-by-case basis.

5. Conclusions

We have advanced the two-dimensional Green function approach of Pétrélis *et al.* (2006) to study internal tide generation by realistic sea-floor topography in realistic stratifications, within the confines of the WKB approximation. For both isolated and double-ridge systems, geometric asymmetry results in asymmetrically radiated internal tides with both the magnitude of the energy flux and the modal content of the wave fields being quite sensitive around criticality. The wave field radiated by a double ridge is very sensitive to the relative position and size of the ridges due to interference between the wave fields they generate and the reflection of wave beams from supercritical slopes. Case studies of the Hawaiian Ridge and Luzon Strait find good qualitative, and in some cases quantitative, agreement between theory and corresponding numerical simulations and field data. For example, the analytical model is able to reasonably predict the low-mode content and asymmetry of the internal tide generated at French Frigate Shoals and the Kaena Ridge. We conclude that this approach can be a useful tool for obtaining oceanographically relevant predictions, provided one recognizes the inevitable limitations in regard to complex topography and very large depth ratios, where three-dimensionality and nonlinearity become important.

An interesting scenario, arising naturally in these studies, is that an appropriately configured double-ridge system can trap internal tide rays between the two ridges, focusing them onto an internal wave attractor. The phenomenon of an internal wave attractor has previously only been studied in a closed container (Maas *et al.* 1997; Hazelwinkel *et al.* 2008; Grisouard, Staquet & Pairaud 2008). The double-ridge configuration is qualitatively different from these previous studies as it has open boundaries through which internal tidal rays can escape. Thus, somewhere like Luzon Strait is conducive to the possibility of an internal wave attractor. This interesting development is the subject of a follow-up paper (Echeverri *et al.* 2010).

Appendix. Numerical evaluation of $\gamma(X)$

Substituting the Green function (2.10) into the boundary condition (2.13) and exchanging the order of summation and integration yields

$$\frac{\pi h(X)}{H} = \sum_{p=1}^{\infty} \frac{1}{p\pi} \frac{\sin(p\hat{h}(X))}{\sqrt{\mathcal{N}(R(\hat{h}(X)))}} \int_{-a}^{b} \gamma(X') \frac{\sin(p\hat{h}(X'))}{\sqrt{\mathcal{N}(R(\hat{h}(X')))}} e^{ip|X-X'|} \, dX'. \qquad (A\,1)$$

To solve (A 1) for $\gamma(X)$, the domain $X \in [-a : b]$ is discretized into $K - 1$ intervals so that $X_1 = -a$ and $X_K = b$. Functions of X are approximated as constants over the small intervals $\Delta X = X_{n+1} - X_n$, such that

$$\int_{X_n}^{X_{n+1}} h(X)\,\mathrm{d}X \approx h_{n+1/2}\Delta X \tag{A 2}$$

and

$$\int_{X_n}^{X_{n+1}} \gamma(X)\,\mathrm{d}X \approx \gamma_{n+1/2}\Delta X, \tag{A 3}$$

where the notation $n + 1/2$ indicates a mid-point value. Therefore, the integral of (A 1) over the interval $[X_n : X_{n+1}]$ yields

$$\frac{\pi h_{n+1/2}}{H}\Delta X \approx \frac{1}{\pi}\sum_{p=1}^{\infty} p^{-1}\int_{X_n}^{X_{n+1}}\int_{-a}^{b} \frac{\sin(p\hat{h}(X))}{\sqrt{\mathcal{N}(R(\hat{h}(X)))}}\frac{\sin(p\hat{h}(X'))}{\sqrt{\mathcal{N}(R(\hat{h}(X')))}}\mathrm{e}^{\mathrm{i}p|X-X'|}\gamma(X')\,\mathrm{d}X'\,\mathrm{d}X. \tag{A 4}$$

Rewriting the inner integral as a sum of integrals over each discrete interval gives

$$\frac{\pi h_{n+1/2}}{H}\Delta X \approx \frac{1}{\pi}\sum_{p=1}^{\infty} p^{-1}\int_{X_n}^{X_{n+1}}\sum_{j=1}^{K-1}\gamma_{j+1/2}$$

$$\times \int_{X_j}^{X_{j+1}} \frac{\sin(p\hat{h}(X))}{\sqrt{\mathcal{N}(R(\hat{h}(X)))}}\frac{\sin(p\hat{h}(X'))}{\sqrt{\mathcal{N}(R(\hat{h}(X')))}}\mathrm{e}^{\mathrm{i}p|X-X'|}\,\mathrm{d}X\,\mathrm{d}X', \tag{A 5}$$

which can be simplified as

$$\frac{\pi h_{n+1/2}}{H}\Delta X = \sum_{j=1}^{K-1} M_{nj}\gamma_{j+1/2}, \tag{A 6}$$

where

$$M_{nj} = \frac{1}{\pi}\sum_{p=1}^{\infty} p^{-1}\int_{X_n}^{X_{n+1}}\int_{X_j}^{X_{j+1}} \frac{\sin(p\hat{h}(X))}{\sqrt{\mathcal{N}(R(\hat{h}(X)))}}\frac{\sin(p\hat{h}(X'))}{\sqrt{\mathcal{N}(R(\hat{h}(X')))}}\mathrm{e}^{\mathrm{i}p|X-X'|}\,\mathrm{d}X\,\mathrm{d}X'. \tag{A 7}$$

The task of evaluating M_{nj} can be simplified. Firstly, it can be seen that

$$M_{nj} = M_{jn}. \tag{A 8}$$

Secondly, for $X > X'$, M_{nj} can be rewritten as

$$M_{nj} = \frac{1}{\pi}\sum_{p=1}^{\infty} p^{-1}\int_{X_n}^{X_{n+1}} \frac{\sin(p\hat{h}(X))}{\sqrt{\mathcal{N}(R(\hat{h}(X)))}}\mathrm{e}^{\mathrm{i}pX}\,\mathrm{d}X\int_{X_j}^{X_{j+1}} \frac{\sin(p\hat{h}(X'))}{\sqrt{\mathcal{N}(R(\hat{h}(X')))}}\mathrm{e}^{-\mathrm{i}pX'}\,\mathrm{d}X'. \tag{A 9}$$

Defining

$$U_n(p) = \int_{X_n}^{X_{n+1}} \frac{\sin(p\hat{h}(X'))}{\sqrt{\mathcal{N}(R(\hat{h}(X')))}}\mathrm{e}^{\mathrm{i}pX'}\,\mathrm{d}X', \tag{A 10}$$

then, for $n \geqslant j + 1$,

$$M_{nj} = \frac{1}{\pi}\sum_{p=1}^{\infty} p^{-1}U_n(p)U_j^*(p). \tag{A 11}$$

Similarly, for $X < X'$ (i.e. $n + 1 \leqslant j$), then

$$M_{nj} = \frac{1}{\pi} \sum_{p=1}^{\infty} p^{-1} U_n^*(p) U_j(p). \tag{A 12}$$

Therefore, evaluating $U_n(p)$ is enough to evaluate M_{nj} for $n \neq m$. The expression for M_{nn} is more complicated and found using symbolic math in MATLAB. For convenience, we first define the slope $s = \mathrm{d}\hat{h}/\mathrm{d}X$ and the following variables:

$$t_1 = 2p\hat{h}_{1/2} + ps_{1/2}\Delta X$$

and

$$t_2 = ps_{1/2}\Delta X - 2p\hat{h}_{1/2},$$

where the subscript $1/2$ is used as a short-hand notation for $n + 1/2$. The diagonal elements of the matrix can be found using

$$M_{nn} = \sum_{p=1}^{\infty} \frac{2\left(1 - s_{1/2}^2\right)^2}{p^3 \pi \mathcal{N}(R(\hat{h}_{1/2})) s_{1/2}} [A + B + C + D + E], \tag{A 13}$$

where

$$\left. \begin{aligned} A &= 2s_{1/2} \left[ip\Delta X \left(1 - s_{1/2}^2\right) + 1 + s_{1/2}^2 \right], \\ B &= \left[i\sin(t_1) + s_{1/2}\cos(t_1) \right] \left(1 - s_{1/2}^2\right), \\ C &= 4is_{1/2}^2 e^{ip\Delta X} \sin(ps_{1/2}\Delta X), \\ D &= 2s_{1/2} e^{ip\Delta X} \left[\cos\left(2p\hat{h}_{1/2}\right)\left(1 - s_{1/2}^2\right) - \left(1 + s_{1/2}^2\right)\cos(ps_{1/2}\Delta X) \right] \end{aligned} \right\} \tag{A 14}$$

and

$$E = \left[i\sin(t_2) + s_{1/2}\cos(t_2) \right] \left(s_{1/2}^2 - 1\right). \tag{A 15}$$

REFERENCES

ALTHAUS, A. M., KUNZE, E. & SANFORD, T. B. 2003 Internal tide radiation from Mendocino Escarpment. *J. Phys. Oceanogr.* **33**, 1510–1527.

BAINES, P. G. 1973 The generation of internal tides by flat-bump topography. *Deep Sea Res.* **20**, 179–205.

BAINES, P. G. 1982 On internal tide generation models. *Deep Sea Res.* **29**, 307–338.

BALMFORTH, N. J., IERLEY, G. R. & YOUNG, W. R. 2002 Tidal conversion by subcritical topography. *J. Phys. Oceanogr.* **32**, 2900–2914.

BALMFORTH, N. J. & PEACOCK, T. 2009 Tidal conversion by supercritical topography. *J. Phys. Oceanogr.* **39**, 1965–1974.

BECKER, J. J., SANDWELL, D. T., SMITH, W. H. F., BRAUD, J., BINDER, B., DEPNER, J., FABRE, D., FACTOR, J., INGALLS, S., KIM, S.-H., LADNER, R., MARKS, K., NELSON, S., PHARAOH, A., SHARMAN, G., TRIMMER, R., VONROSENBURG, J., WALLACE, G. & WEATHERALL, P. 2009 Global bathymetry and elevation data at 30 arc seconds resolution: SRTM30_PLUS. *Marine Geodesy* **32** (4), 355–371.

BELL, T. H. 1975 Lee waves in stratified flows with simple harmonic time dependence. *J. Fluid Mech.* **67**, 705–722.

CARTER, G. S., MERRIFIELD, M. A., BECKER, J. M., KATSUMATA, K., GREGG, M. C., LUTHER, D. S., LEVINE, M. D., BOYD, T. J. & FIRING, Y. L. 2008 Energetics of M2 barotropic-to-baroclinic tidal conversion at the Hawaiian islands. *J. Phys. Oceanogr.* **38**, 2205–2223.

CHAO, S. Y., KO, D. S., LIEN, R. C. & SHAW, P. T. 2007 Assessing the west ridge of Luzon Strait as an internal wave mediator. *J. Oceanogr.* **63**, 897–911.

Echeverri, P., Flynn, M. R., Winters, K. B. & Peacock, T. 2009 Low-mode internal tide generation by topography: an experimental and numerical investigation. *J. Fluid Mech.* **636,** 91–108.

Echeverri, P., Yokossi, T., Balmforth, N. J. & Peacock, T. 2010 Internal tide attractors in double ridges. *J. Fluid Mech.* (submitted).

Egbert, G. D. & Ray, R. D. 2000 Significant dissipation of tidal energy in the deep ocean inferred from satellite altimeter data. *Nature* **405**, 775–778.

Farmer, D. M., Li, Q. & Park, J. 2009 Internal wave observations in the South China Sea: the role of rotation and nonlinearity. *Atmos. Ocean* **47** (4), 267–280.

Garrett, C. & Kunze, E. 2007 Internal tide generation in the deep ocean. *Annu. Rev. Fluid Mech.* **39**, 57–87.

Griffiths, S. D. & Grimshaw, R. H. J. 2007 Internal tide generation at the continental shelf modeled using a modal decomposition: two-dimensional results. *J. Phys. Oceanogr.* **37**, 428–451.

Grisouard, N., Staquet, C. & Pairaud, I. 2008 Numerical simulation of a two-dimensional internal wave attractor. *J. Fluid Mech.* **614**, 1–14.

Hawaii Mapping Research Group 2009 Main Hawaiian Islands multibeam synthesis. http://www.soest.hawaii.edu/HMRG/Multibeam/index.php.

Hawaiian Ocean Time-series 2009 http://hahana.soest.hawaii.edu/hot/hot_jgofs.html.

Hazewinkel, J., Van Breevoort, P., Dalziel, S. B. & Maas, L. R. M. 2008 Observations on the wavenumber spectrum and evolution of an internal wave attractor. *J. Fluid Mech.* **598**, 373–382.

Jan, S., Lien, R. C. & Ting, C. H. 2008 Numerical study of baroclinic tides in Luzon Strait. *J. Oceanogr.* **64**, 789–802.

Khatiwala, S. 2003 Generation of internal tides in an ocean of finite depth: analytical and numerical calculations. *Deep Sea Res.* **50**, 3–21.

Klymak, J. M., Moum, J. N., Nash, J. D., Kunze, E., Griton, J. B., Carter, G. S., Lee, C. M., Sanford, T. B. & Gregg, M. C. 2006 An estimate of tidal energy lost to turbulence at the Hawaiian Ridge. *J. Phys. Oceanogr.* **36**, 1148–1164.

Klymak, J. M., Pinkel, R. & Rainville, L. 2008 Direct breaking of the internal tide near topography: Kaena Ridge, Hawaii. *J. Phys. Oceanogr.* **38** (2), 380–399.

Lee, C. M., Kunze, E., Sanford, T. B., Nash, J. D., Merrifield, M. A. & Holloway, P. E. 2006 Internal tides and turbulence along the 3000-m isobath of the Hawaiian ridge. *J. Phys. Oceanogr.* **36**, 1165–1183.

Llewellyn Smith, S. G. & Young, W. R. 2002 Conversion of the barotropic tide. *J. Phys. Oceanogr.* **32**, 1554–1566.

Llewellyn Smith, S. G. & Young, W. R. 2003 Tidal conversion at a very steep ridge. *J. Fluid Mech.* **495**, 175–191.

Maas, L. R. M., Benielli, D., Sommeria, J. & Lam, F. P. A. 1997 Observation of an internal wave attractor in a confined stably-stratified fluid. *Nature* **388**, 557–561.

Merrifield, M. A. & Holloway, P. E. 2002 Model estimates of M2 internal tide energetics at the Hawaiian ridge. *J. Geophys. Res.* **107** (C8), 3179–3190.

Nash, J. D., Kunze, E., Lee, C. M. & Sanford, T. B. 2006 Structure of the baroclinic tide generated at Kaena Ridge, Hawaii. *J. Phys. Oceanogr.* **36**, 1123–1135.

National Geophysical Data Center, National Oceanic and Atmospheric Administration, U.S. Department of Commerce 2006 2-minute gridded global relief data (ETOPO2v2). http://www.ngdc.noaa.gov/mgg/fliers/06mgg01.html.

Niwa, Y. & Hibiya, T. 2004 Three-dimensional numerical simulation of M2 internal tides in the East China Sea. *J. Geophys. Res.* **109**, C04027.

Nycander, J. 2005 Generation of internal waves in the deep ocean. *J. Geophys. Res.* **110**, C10028.

Nycander, J. 2006 Tidal generation of internal waves from a periodic array of steep ridges. *J. Fluid Mech.* **567**, 415–432.

Pétrélis, F., Llewellyn Smith, S. G. & Young, W. R. 2006 Tidal conversion at a submarine ridge. *J. Phys. Oceanogr.* **36**, 1053–1071.

Rainville, L. & Pinkel, R. 2006 Baroclinic energy flux at the Hawaiian ridge: observations from the R/P FLIP. *J. Phys. Oceanogr.* **36**, 1104–1122.

Ray, R. D. & Mitchum, G. T. 1997 Surface manifestation of internal tides in the deep ocean: Observations from altimetry and island gauges. *Prog. Oceanogr.* **40**, 135–162.

Robinson, R. M. 1969 The effects of a barrier on internal waves. *Deep Sea Res.* **16**, 421–429.

Rudnick, D. L., Boyd, T. J., Brainard, R. E., Carter, G. S., Egbert, G. D., Gregg, M. C., Holloway, P. E., Klymak, J. M., Kunze, E., Lee, C. M., Levine, M. D., Luther, D. S., Martin, J. P., Merrifield, M. A., Moum, J. N., Nash, J. D., Pinkel, R., Rainville, L. & Sanford, T. B. 2003 From tides to mixing along the Hawaiian ridge. *Science* **301**, 355–357.

Simmons, H. L., Hallberg, R. W. & Arbic, B. K. 2004 Internal wave generation in a global baroclinic tide model. *Deep Sea Res.* **51**, 3043–3068.

St Laurent, L., Stringer, S., Garrett, C. & Perrault-Joncas, D. 2003 The generation of internal tides at abrupt topography. *Deep Sea Res.* **50** (8), 987–1003.

St Laurent, L. C. & Nash, J. D. 2004 An examination of the radiative and dissipative properties of deep ocean internal tides. *Deep Sea Res.* **51**, 3029–3042.